Electrostatic Modulation and Mechanism of the Electronic Properties of Monolayer MoS$_2$ via Ferroelectric BiAlO$_3$(0001) Polar Surfaces

Jin Yuan, Jian-Qing Dai,* and Cheng Ke

ACCESS | Metrics & More | Article Recommendations | SI Supporting Information

ABSTRACT: In the present work, first-principles density functional theory calculations were carried out to explore the intrinsic interface coupling and electrostatic modulation as well as the effect of ferroelectric polarization reversal in the MoS$_2$/BiAlO$_3$(0001) [MoS$_2$/BAO(0001)] hybrid system. In addition to the interaction mechanism of the large ionic−van der Waals (vdW) coupling, our results indicate that the electronic properties of monolayer MoS$_2$ on the BAO(0001) polar surface can be effectively modulated by reversing the ferroelectric polarization and/or engineering the domain structures of the substrate. Due to the unusual charge transfer between the MoS$_2$ overlayer and the down-polarized ferroelectric BAO(0001) substrate, in the final analysis, the physical mechanism determining the interfacial charge transfer in the MoS$_2$/BAO(0001) hybrid system is attributed to the specific band alignment between the clean BAO(0001) surface and the freestanding monolayer MoS$_2$. Furthermore, our study predicts that MoS$_2$-based ferroelectric field-effect transistors and various types of seamless p−i, n−i, p−n, p$^+$−p, and n$^+$−n homojunctions possessing an extremely steep built-in electric field can be fabricated by reversing the ferroelectric polarization and/or patterning the domain structure of the BAO(0001) substrate.
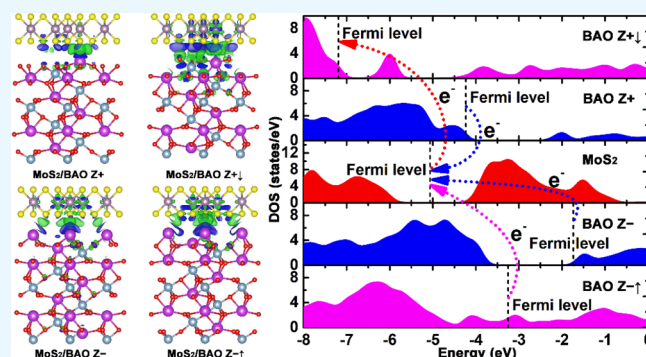
1. INTRODUCTION

For low-power logic applications and nonvolatile memory, ferroelectric field-effect transistors (FeFETs) based on a two-dimensional (2D) channel and ferroelectric gating are very attractive candidates owing to the switchable electric polarization and high dielectric constant of ferroelectric materials.[1−5] Back in 2010, an experimental study reported that such graphene-based FeFETs fabricated on a ferroelectric Pb(Zr$_{0.2}$Ti$_{0.8}$)O$_3$ substrate show an unusual resistance hysteresis.[6] Subsequently, FeFETs with a 2D van der Waals (vdW) transition-metal dichalcogenide MX$_2$ (M = Mo and W; X = S, Te, and Se) channel have also been experimentally demonstrated.[2,3,7−12] Furthermore, a recent experimental investigation revealed that p−n homojunctions in a MoTe$_2$ monolayer can be obtained using a periodically polarized ferroelectric P(VDF−TrFE) substrate.[13] The integration of 2D monolayers with ferroelectric materials is becoming a hot research subject, as it offers the possibility to develop novel devices for nanoelectronic and optoelectronic applications. To realize practical applications, gaining an atomic-scale understanding of the intrinsic interface coupling as well as electrostatic modulation in 2D/ferroelectric hybrid systems is the first step.

As a representative member of the family of 2D vdW MX$_2$ materials, monolayer MoS$_2$ has attracted intensive attention from researchers.[2,3,7,11,12] In addition to possessing optoelectronic and electronic properties similar or even superior to those of graphene, monolayer MoS$_2$ is a semiconductor with a direct band gap of 1.90 eV, which renders it widely applicable to investigate photocatalyst processes and optoelectronic nanodevices.[2,3,7,11,12,14] In experiments, monolayer MoS$_2$ can be prepared via chemical vapor deposition (CVD), hydrothermal synthesis, liquid-phase stripping, and mechanical stripping methods.[15−17] Furthermore, owing to its unique electronic structure and high flexibility, monolayer MoS$_2$ is also considered as a promising candidate to explore flexible electronic devices.[18]

Ferroelectric BiAlO$_3$ (BAO) with the R3c space group exhibits outstanding piezoelectric and ferroelectric properties along the [0001] direction and is a promising alternative material to the lead-based Pb(Zr, Ti)O$_3$ (PZT) piezoelectric material.[19−21] The theoretical spontaneous polarization of BAO is about 80 μC/cm^2.[22] Epitaxial BAO thin films can be

fabricated using the pulsed laser deposition (PLD) method.[23] In addition, a recent theoretical study[24] indicated that due to the coexistence and coupling of bulk Rashba spin-splitting and ferroelectricity, bulk BAO can be an attractive ferroelectric Rashba semiconductor. Note that in our previous reports[22,25] regarding BAO(0001) polar surfaces, the thermodynamic surface phase diagram and the corresponding electronic properties and spin textures were determined. It was found that the thermodynamically preferred positive (Z+) and negative (Z−) polar surfaces are terminated by the −Al− O_3−Bi atomic layer and the −O_3−Bi_2 layer, respectively. Note that the BAO Z+ and Z− surfaces represent the spontaneous polarization pointing toward and away from the surface termination, respectively.

In this work, by integrating monolayer MoS_2 with the ferroelectric BAO(0001) polar surface, the intrinsic interface coupling as well as electrostatic modulation in the MoS_2/BAO(0001) heterostructure was studied via first-principles density functional theory (DFT) calculations. The results exhibit that in addition to the unusual charge transfer opposite the polarization compensation mechanism, the electronic properties of monolayer MoS_2 adsorbed onto the BAO(0001) substrate can be effectively modulated by reversing the ferroelectric polarization and/or patterning the domain structure. Regarding the band alignment between the clean BAO(0001) polar surface and the freestanding monolayer MoS_2, the physical mechanism behind the interfacial charge transfer is well explained. Our research provides theoretical evidence for the fabrication of FeFETs based on MoS_2/BAO(0001) heterostructures as well as various types of p−i, n−i, p−n, p^+−p, and n^+−n homojunctions in monolayer MoS_2 on the ferroelectric BAO(0001) polar surface by reversing the ferroelectric polarization and/or patterning the domain structure.

2. METHODOLOGY

All first-principles DFT calculations with the projector augmented wave (PAW) potentials were simulated using the Vienna ab initio simulation package (VASP).[26] The exchange−correlation functionals were described via the Perdew−Burke−Ernzerhof form revised for solids (PBEsol) of the generalized gradient approximation (GGA), which has been confirmed to be very precise in predicting the spontaneous polarization of ferroelectric materials.[27−29] To consider the weak interactions existing between the BAO(0001) polar surface and monolayer MoS_2, the dispersion-corrected DFT-D3 method was employed.[30] The Bi $5d^{10}6s^26p^3$, Al $3s^23p^1$, O $2s^22p^4$, Mo $4p^64d^55s^1$, and S $3s^23p^4$ electrons were treated as valence electrons. In the structural optimization and self-consistent calculations, the Brillouin zone was sampled with a Đ-centered 5 × 5 × 1 k-point mesh. However, for the calculations of the density of states (DOS) and electronic band structures, a Đ-centered 11 × 11 × 1 k-point mesh and a dense k-point string of ∼250 points per Å$^{−1}$ were employed, respectively. Furthermore, to quantitatively evaluate the charge transfer between the BAO(0001) surface and monolayer MoS_2, the Bader topological charge analysis with a Đ-centered 11 × 11 × 1 k-point mesh was also carried out.[31] The cutoff energy of the plane wave expansion and the convergence criterion of the energy were set to 500 and $10^{−6}$ eV, respectively. Importantly, the dipole correction was turned on to counteract the interaction between periodic slab images.[32] Due to the existence of a prominent Rashba−Dresselhaus spin-splitting

in the BAO(0001) polar surface and bulk,[24,25] the influence of the spin−orbit coupling (SOC) on the obtained results and conclusions was also investigated.

For monolayer MoS_2 and the BAO(0001) substrate, the calculated lattice constants were 3.140 and 5.363 Å, respectively, which are consistent with those obtained in previous reports.[24,33] The MoS_2/BAO(0001) hybrid system with a vacuum layer with thickness > 20 Å was constructed by placing the $\sqrt{3} \times \sqrt{3}$ MoS_2 supercell on the 1 × 1 BAO(0001) slab. Due to the ∼1% lattice mismatch between the $\sqrt{3} \times \sqrt{3}$ MoS_2 supercell and the 1 × 1 BAO(0001) slab, the lattice constant of the BAO(0001) slab was increased to match that of the MoS_2 supercell so that no strain is introduced into the MoS_2 overlayer. The BAO Z+ and Z− slabs as well as the polarization-reversed BAO Z+ (denoted as BAO Z+↓) and Z− (denoted as BAO Z−↑) slabs were constructed via surface termination and the six −Al−O_3−Bi− trilayers. For the MoS_2/BAO(0001) hybrid system, in addition to the full structural optimization of the surface termination and the two outer −Al−O_3−Bi− trilayers, fully atomic relaxations were performed on the MoS_2 overlayer until the residual force appearing on each atom was less than 0.01 eV/Å. The in-plane lattice constants and atomic positions of the backside of the BAO(0001) slabs were fixed. In addition, as shown in Figure S1, the five typical interfacial configurations between the BAO Z± surface and monolayer MoS_2 were explored. In terms of the calculated total energy for the relaxed MoS_2/BAO Z+ and Z− heterostructures, the preferred adsorption configuration respectively exhibits lower total energies by about 306 and 328 meV/supercell (0.19 and 0.21 J/m^2) than the configuration with the highest energy. The top views of this energetically preferred adsorption configuration are plotted in Figure S1b,g, respectively. Further calculations were carried out, choosing the interfacial configurations with the lowest total energy.

3. RESULTS AND DISCUSSION

3.1. Freestanding Monolayer MoS_2. As mentioned in the introduction, monolayer MoS_2 exhibits distinctive optical, electronic, and catalytic properties and is a direct band-gap semiconductor.[14] Previous theoretical and experimental results[14,34] showed that the band gap of monolayer MoS_2 is 1.90 eV. To check our calculated results using the DFT−PBEsol approach, the obtained lattice constants of monolayer MoS_2 ($a = b = 3.140$ Å) were compared with the value of 3.160 Å reported in ref 33. Such a small error is perfectly acceptable for first-principles calculations. The calculated lattice constants of the BAO(0001) substrate ($a = b = 5.363$ Å) are also in good agreement with the value of 5.375 Å obtained in a previous experimental result.[19] Therefore, the DFT−PBEsol approach seems to be a reasonable choice for these calculations.

Next, we focus on the electronic properties of the freestanding monolayer MoS_2. Figure 1a,c describes the electronic band structures of the primitive cell of the freestanding monolayer MoS_2 without SOC and with SOC, respectively. Obviously, monolayer MoS_2 exhibits the characteristics of a direct band-gap material as the valence band maximum (VBM) and conduction band minimum (CBM) are both located at the K point in the Brillouin zone. The band gaps without SOC and with SOC are respectively 1.79 and 1.71 eV, which are only about 0.11−0.19 eV less than a previously reported experimental value.[14] Due to the usual underestimation of the band gap obtained with the PBE
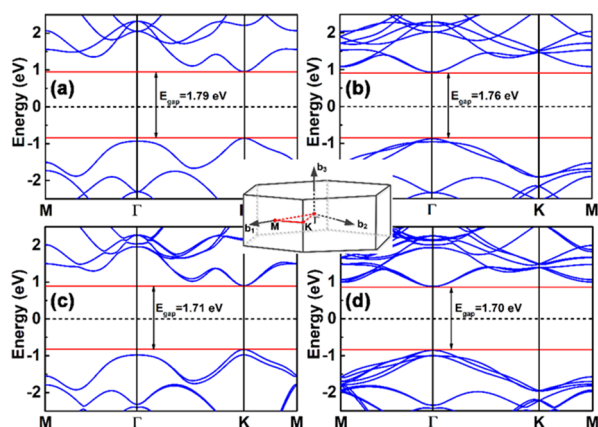
Figure 1. (a, c) Band structures of the freestanding monolayer MoS_2 primitive cell without SOC and with SOC, respectively. (b, d) Band structures of the freestanding monolayer MoS_2 $\sqrt{3} \times \sqrt{3}$ supercell without SOC and with SOC, respectively. The Fermi level is indicated by a black short dashed line. The inset exhibits the first Brillouin zone of the hexagonal supercell.

functional,[29] such a difference in the band gap is still within an acceptable range. Figure 1b,d shows the electronic band structures of the $\sqrt{3} \times \sqrt{3}$ supercell of the freestanding monolayer MoS_2 without SOC and with SOC, respectively. It can be seen that in addition to the negligible change in the band gap with respect to that in the primitive cell in the Brillouin zone, the K point in the primitive cell in the Brillouin zone is folded into the Γ point in the $\sqrt{3} \times \sqrt{3}$ supercell in the Brillouin zone. Furthermore, by comparing the band structures without SOC and with SOC, another interesting phenomenon can be found, i.e., the band gap for the case with SOC is slightly decreased by about 0.06–0.08 eV relative to that without SOC due to band-splitting.[35]

3.2. The MoS_2/BAO Z+ and Z+↓ Heterostructures. This section focuses on the interface coupling and electrostatic modulation in the MoS_2/BAO Z+ heterostructure as well as the effect of polarization reversal. The side views of the atomic structures for the relaxed $\sqrt{3} \times \sqrt{3}/1 \times 1$ MoS_2/BAO Z+ and Z+↓ heterostructures are illustrated in Figure 2. It can be observed that after full structure relaxation, the BAO Z+ substrate is still terminated with the −Al−O₃−Bi atomic layer (as shown in Figure 2a), which is the same as the initial thermodynamically preferred BAO Z+ surface termination without MoS_2 adsorption.[22,25] Such information indicates that
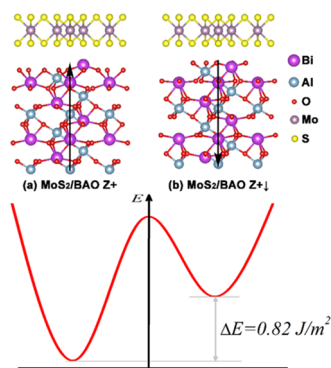
the adsorption of MoS_2 has no significant influence on the atomic structures of the BAO Z+ surface. Similar conclusions can also be obtained for the relaxed MoS_2/BAO Z+↓ heterostructure (as shown in Figure 2b). Note that the MoS_2/BAO Z+↓ heterostructure was constructed without changing the surface chemical composition of the BAO Z+ substrate; only the ferroelectric polarization was reversed. In addition, Figure 2 displays the energy difference (ΔE) of the potential well for the $\sqrt{3} \times \sqrt{3}/1 \times 1$ MoS_2/BAO Z+ and Z+↓ heterostructures. The ΔE value of 0.82 J/m² indicates that the MoS_2/BAO Z+ hybrid system is more stable than the MoS_2/BAO Z+↓ system due to the lowest surface free energy of the thermodynamically preferred surface termination.

For the relaxed MoS_2/BAO Z+ and Z+↓ heterostructures, the calculated layer spacings (d_{S-BAO}) between the BAO substrate and monolayer MoS_2 are respectively 2.59 and 2.35 Å (as listed in Table 1), which are much bigger than the interface spacing (0.11–0.76 Å) of the metal−oxide contact.[36] According to ref 37, the vdW gap (g_{vdW}) could be approximated as $g_{vdW} \approx d_{vdW} - r_a - r_b$, where d_{vdW} and r_a (or r_b) represent the vdW distance and covalent radii of individual atoms, respectively. In the case of the investigated MoS_2/BAO Z+ and Z+↓ heterostructures, the g_{vdW} is defined as $g_{vdW} \approx d_{S-BAO} - r_{Bi} - r_S$ and $g_{vdW} \approx d_{S-BAO} - r_O - r_S$, respectively. Therefore, the calculated g_{vdW} values for the MoS_2/BAO Z+ and Z+↓ heterostructures are 0.11 and 0.60 Å, respectively, which are much smaller than the g_{vdW} value of 1.80 Å obtained for bulk MoS_2.[37] Furthermore, being an important parameter to investigate the interface coupling mechanism, the binding energy (W_b) between the BAO substrate and monolayer MoS_2 was calculated according to $W_b = -(E_{MoS2/BAO} - E_{MoS2} - E_{BAO})/S$, where $E_{MoS2/BAO}$, E_{MoS2} (E_{BAO}), and S respectively indicate the total energy of the MoS_2/BAO heterostructure, the total energy of the MoS_2 isolated monolayer (BAO substrate) with fixed atomic positions in the MoS_2/BAO system, and the area of the 1×1 BAO(0001) surface unit cell. As listed in Table 1, the binding energies of the MoS_2/BAO Z+ and Z+↓ heterostructures are 5.63 and 5.98 J/m², respectively. In contrast with pure vdW interactions of about 0.19 J/m² (0.34 J/m²) in bulk MoS_2 (graphite),[38,39] the values obtained in the present study are an order of magnitude higher. Due to the much smaller g_{vdW} value and much bigger W_b value, it is reasonable to assume that the interface interaction mechanism of the MoS_2/BAO Z+ and Z+↓ heterostructures is not only the pure vdW coupling.

Figure 3 shows the side views of the electron localization functions (ELFs) and differential charge densities for the MoS_2/BAO Z+ and Z+↓ heterostructures to further investigate the interface coupling mechanism.[40,41] Due to the included Pauli repulsion effect, the ELFs could be directly employed to observe the nature of the three-dimensional bonding. For the MoS_2 overlayer adsorbed at the BAO Z+ and Z+↓ surfaces, as shown in Figure 3a,b, the electron cloud of the interfacial S atomic layer shows a clear deformation with respect to the freestanding monolayer MoS_2 (not shown). Moreover, compared with the ELFs of the clean BAO Z+ and Z+↓ surfaces (as shown in Figure S6a,b), it can be seen that the 6s lone-pair electron of the interfacial Bi atom in the MoS_2/BAO Z+ heterostructure disappears. The above information indicates that the electronic properties of monolayer MoS_2 are effectively modulated by the ferroelectric BAO Z+ and Z+↓ surfaces. Additionally, there is no shared electron cloud (bond

Figure 2. (a, b) Side views of atomic structures and energy difference (ΔE) of the potential well for $\sqrt{3} \times \sqrt{3}/1 \times 1$ MoS_2/BAO Z+ (a) and Z+↓ (b) heterostructures.

Table 1. Layer Spacing ($d_{\text{S-BAO}}$) and Binding Energy (W_b) between the BAO Substrate and Monolayer MoS$_2$ and the Change in Charge in the Interfacial S Atomic Layer (ΔQ_S), Mo Layer (ΔQ_{Mo}), and Monolayer MoS$_2$ (ΔQ_{tot}) with Respect to the Freestanding Monolayer MoS$_2$ as well as the Carrier Density n in the MoS$_2$ Overlayer on BAO(0001) Substrates[a]

	$d_{\text{S-BAO}}$ (Å)	W_b (J/m^2)	ΔQ_S (e)	ΔQ_{Mo} (e)	ΔQ_{tot} (e)	n (10^{13} cm^{-2})
MoS$_2$/BAO Z+	2.59	5.63	0.049	0.022	0.067	−2.62
MoS$_2$/BAO Z+↓	2.35	5.98	−0.197	−0.003	−0.199	+7.77
MoS$_2$/BAO Z−	2.67	6.22	0.223	0.035	0.251	−9.80
MoS$_2$/BAO Z−↑	2.48	6.21	0.282	0.060	0.332	−12.96

[a]Note that the negative (positive) sign of n denotes an electron (hole) carrier.
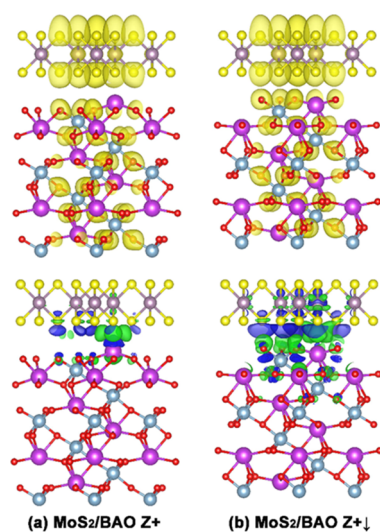

Figure 3. (a, b) Side views of ELFs and differential charge densities for MoS$_2$/BAO Z+ (a) and Z+↓ (b) heterostructures. The blue and green colors in differential charge density images respectively represent the gain of holes and electrons. Note that the ELFs and differential charge density maps are plotted for the isosurfaces of 0.7 and 9×10^{-4} e/Å^3, respectively. The symbols of Bi, Al, O, Mo, and S atoms are shown in Figure 2.

attractors) in both the MoS$_2$/BAO Z+ and Z+↓ interfaces, which rules out the possibility of covalent coupling in the MoS$_2$/BAO Z+ and Z+↓ interfaces. Indeed, according to ref 42, the interface interaction mechanism in the MoS$_2$/BAO Z+ and Z+↓ hybrid systems should be defined as an ionic−vdW coupling combining electrostatic interactions with vdW interactions. From the differential charge densities of the MoS$_2$/BAO Z+ and Z+↓ interfaces (as shown in Figure 3a,b), the remarkable charge transfer does indicate the nature of the electrostatic interactions, i.e., the characteristics of the ionic type. In addition to the significant charge transfer observed, the differential charge density images indicate that the MoS$_2$ overlayer adsorbed onto the BAO Z+ and Z+↓ surfaces shows a gain in electrons and holes, respectively, which suggests possible corresponding n- and p-type doping in this MoS$_2$ overlayer.

To confirm the respective n- and p-type doping in the MoS$_2$ overlayer adsorbed onto the BAO Z+ and Z+↓ substrates, the Bader topological charge analysis[31] with an accuracy exceeding 10^{-3} e was employed to quantitatively estimate the interfacial charge transfer. As presented in Table 1 for the MoS$_2$ overlayer on the BAO Z+ surface, the interfacial S atomic layer, Mo layer, and monolayer MoS$_2$ were calculated to gain charges of 0.049, 0.022, and 0.067 e, respectively, per supercell surface area relative to the freestanding monolayer MoS$_2$. This is equivalent to electrostatic n-type doping with a carrier density

of $n_e = 2.62 \times 10^{13}$ cm^{-2}. However, for the MoS$_2$ overlayer on the BAO Z+↓ surface, the situation is different. The results of the Bader topological charge analysis indicate that the interfacial S atomic layer, Mo layer, and monolayer MoS$_2$ lost 0.197, 0.003, and 0.199 e, respectively, per supercell surface area relative to the freestanding monolayer MoS$_2$. This corresponds to a p-type carrier density of $n_h = 7.77 \times 10^{13}$ cm^{-2}. We note that the transferred charges in the MoS$_2$/BAO Z+ and Z+↓ heterostructures show the same order of magnitude as that of the graphene/BiFeO$_3$(0001) hybrid systems.[43,44] Simultaneously, the calculated carrier density difference between the n- and p-type monolayer MoS$_2$ on the BAO(0001) surface is 1.04×10^{14} cm^{-2}, which is two order magnitudes higher than the theoretical value and experimental observation in graphene/LiNbO$_3$ hybrid structures.[45] Due to the significant change in resistance in the MoS$_2$ channel before and after the polarization reversal, i.e., the large $I_{\text{on}}/I_{\text{off}}$ ratio, for nanoelectronic and optoelectronic applications, this is a great advantage. More importantly, these results are well consistent with the conclusion obtained from the differential charge density images discussed above, and the more remarkable charge transfer in the MoS$_2$/BAO Z+↓ interface could also be observed in the differential charge density images. In addition, both the differential charge density images and Bader topological charge analysis indicate that the charge transfer mainly involves the interfacial atoms in the MoS$_2$/BAO Z+ and Z+↓ heterostructures. Note that due to the transition from n- to p-type doping in the MoS$_2$ overlayer caused by polarization reversal, the MoS$_2$/BAO(0001) heterostructure could be a promising platform to explore FeFETs based on the MoS$_2$ channel.

The electronic band structures were calculated along high-symmetry directions of the $\sqrt{3} \times \sqrt{3}$ MoS$_2$ supercell in the Brillouin zone for the MoS$_2$/BAO Z+ and Z+↓ heterostructures (without SOC). As shown in Figure 4, the projected band of the MoS$_2$ overlayer on the BAO Z+ surface undergoes a downward shift of 0.38 eV relative to the freestanding monolayer MoS$_2$. By contrast, an upward shift of 0.64 eV with respect to the freestanding monolayer MoS$_2$ can be observed in the projected band of the MoS$_2$ overlayer on the BAO Z+↓ surface. Such a large band offset of 1.02 eV in monolayer MoS$_2$ on the BAO Z+ and Z+↓ substrates implies that significant changes in resistance will occur in the MoS$_2$ overlayer as a consequence of the ferroelectric polarization reversal of the BAO substrate. This is still in good agreement with the above results of Bader's topological charge analysis and the differential charge densities. The charge transfer at the MoS$_2$/BAO Z+ and Z+↓ interfaces can be explained by inspecting the band alignment between the BAO(0001) substrate and monolayer MoS$_2$. As shown in Figure 4 for the MoS$_2$/BAO Z+ heterostructure, the calculated Fermi level of the clean BAO Z+ surface is 4.20 eV below the vacuum level (0
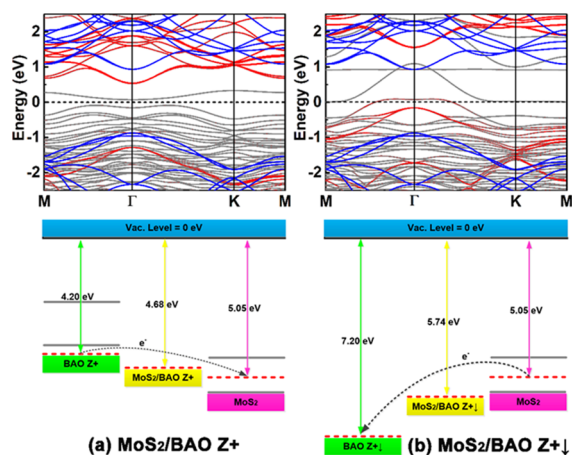
Figure 4. (a, b) Band structures along high-symmetry directions of the $\sqrt{3} \times \sqrt{3}$ MoS$_2$ supercell Brillouin zone and band alignment (vacuum level is set to 0 eV) for MoS$_2$/BAO Z+ (a) and Z+↓ (b) heterostructures (without SOC). The red and blue circle dots correspond to the projected band of the MoS$_2$ overlayer on BAO Z+ and Z+↓ surfaces and the band structure of the freestanding monolayer MoS$_2$, respectively. Both the black and red short dashed lines indicate the Fermi level.

eV) and is 0.85 eV higher than the calculated Fermi level of the freestanding monolayer MoS$_2$. Due to the higher Fermi level with respect to the freestanding monolayer MoS$_2$, the electrons will transfer from the BAO Z+ substrate to the MoS$_2$ overlayer, resulting in electrostatic n-type doping. However, the opposite is true for the MoS$_2$/BAO Z+↓ heterostructure. As the Fermi level is 2.15 eV lower than that of the freestanding monolayer MoS$_2$, the hole carriers in the MoS$_2$ overlayer on the BAO Z+↓ surface are bound to appear. Furthermore, after charge transfer, the Fermi level of the MoS$_2$/BAO Z+ and Z+↓ hetero-structures is exactly in between the clean BAO surface and the freestanding monolayer MoS$_2$, which confirms the above explanation for the charge transfer at the MoS$_2$/BAO Z+ and Z+↓ interfaces.[46] Finally, due to the orbital hybridization with the BAO substrate,[47] the band gap of the MoS$_2$ overlayer on the BAO Z+ and Z+↓ surfaces is also effectively modulated by the BAO(0001) ferroelectric substrate, as shown in Figure 4.

In addition, as mentioned in the introduction, bulk BAO is believed to be an attractive ferroelectric Rashba semiconductor owing to the coexistence and coupling of bulk Rashba spin-splitting and ferroelectricity.[24] In our former report,[25] due to the existence of the heavy element Bi, the BAO(0001) surfaces were also found to exhibit distinctive Rashba−Dresselhaus spin-splittings. It is therefore necessary to explore the influence of SOC on the obtained results and conclusions. Figure S2a,c shows the calculated electronic band structures along high-symmetry directions of the $\sqrt{3} \times \sqrt{3}$ MoS$_2$ supercell in the Brillouin zone for the MoS$_2$/BAO Z+ and Z+↓ hetero-structures (with SOC). Compared with the electronic band structures without SOC, no significant change can be observed in addition to the clear band-splitting of the VBM. Furthermore, Figure S3a−c illustrates the band alignment between the freestanding monolayer MoS$_2$ and the clean BAO Z+ (Z+↓) substrate (with SOC). As expected, the mechanism of band alignment remains valid.

3.3. The MoS$_2$/BAO Z− and Z−↑ Heterostructures.
Similarly, the MoS$_2$/BAO Z−↑ heterostructure was con-structed without changing the surface chemical composition of the BAO Z− substrate; only the ferroelectric polarization

was reversed. As plotted in Figure S4, after full structural optimization, the thermodynamically preferred polarized BAO Z− surface with MoS$_2$ adsorption is still terminated by the −O$_3$−Bi$_2$ atomic layer, and the atomic structure of the polarization-reversed Z− (Z−↑) surface also shows only a slight change. This reveals that the adsorption of MoS$_2$ has no significant influence on the atomic structure of the BAO Z− and Z−↑ surfaces. Such information is consistent with the MoS$_2$/BAO Z+ and Z+↓ heterostructures. The fact that the potential well energy was reduced by 1.68 J/m^2 (as shown in Figure S4) also indicates that the MoS$_2$/BAO Z− system is still more stable than the MoS$_2$/BAO Z−↑ system. According to our previous calculations regarding the thermodynamic surface phase diagram of the BAO(0001) surface,[22] the polarization-reversed BAO Z+ (Z+↓) and Z− (Z−↑) surface terminations should be energetically metastable and will therefore possess higher surface free energy with respect to the thermodynami-cally preferred surface terminations. Such information also implies that to construct a thermodynamically favorable 2D/ ferroelectric hybrid system, using thermodynamically preferred ferroelectric surface termination should be an important prerequisite.

Next, we pay attention to the interface coupling mechanism in the MoS$_2$/BAO Z− and Z−↑ heterostructures. As presented in Table 1 for the MoS$_2$/BAO Z− (MoS$_2$/BAO Z−↑) heterostructure, the layer spacing ($d_{\text{S-BAO}}$) and binding energy (W_b) between the BAO substrate and the MoS$_2$ overlayer are 2.67 Å (2.48 Å) and 6.22 J/m^2 (6.21 J/m^2), respectively. The calculated g_{vdW} values for the MoS$_2$/BAO Z− and Z−↑ heterostructures are 0.19 and 0.00 Å, respectively. These values are very similar to those of the MoS$_2$/BAO Z+ and Z+↓ heterostructures. Combining the ELFs with the differential charge density (as shown in Figures S5 and S6c,d), the interface coupling mechanism in the MoS$_2$/BAO Z− and Z−↑ heterostructures should still be the same ionic−vdW interaction as in the MoS$_2$/BAO Z+ and Z+↓ systems.

Next, we focus on the electrostatic modulation and mechanism of the electronic properties of monolayer MoS$_2$ on the BAO Z− and Z−↑ polar surfaces. As plotted in Figure 5, the projected bands of the MoS$_2$ overlayer on the BAO Z− and Z−↑ surfaces exhibit downward shifts of 0.90 and 0.74 eV, respectively, which indicates that both MoS$_2$ overlayers on the BAO Z− and Z−↑ polar surfaces are electrostatically n-doped. To quantitatively explore the charge doping effect in the MoS$_2$ overlayer adsorbed at the BAO Z− and Z−↑ substrates, the Bader topological charge analysis[31] was employed to estimate precisely the interfacial charge transfer. As listed in Table 1 for the MoS$_2$ overlayer on the BAO Z− (Z−↑) surface, the interfacial S atomic layer, Mo layer, and monolayer MoS$_2$ were found to gain 0.223 (0.282), 0.035 (0.060), and 0.251 e (0.332 e), respectively, per supercell surface area relative to the freestanding monolayer MoS$_2$. This is equivalent to electro-static n-type doping with a carrier density of $n_e = 9.80 \times 10^{13}$ cm^{-2} ($n_e = 12.96 \times 10^{13}$ cm^{-2}). Note that as displayed in Table 1, the carrier density introduced in the MoS$_2$ overlayers on both polarization-unreversed BAO Z+ and Z− surfaces is much lower than that in the polarization-reversed BAO Z+ (Z+↓) and Z− (Z−↑) surfaces. This is due to the characteristics of metastability of the polarization-reversed BAO(0001) surface terminations relative to the thermodynamically preferred polarization-unreversed BAO Z+ and Z− surface terminations.[22] More interestingly, different from the so-called polarization compensation mechanism of ferroelectric
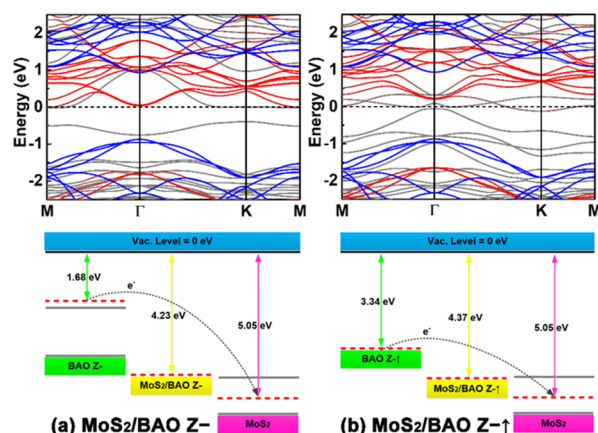
Figure 5. (a, b) Band structures along high-symmetry directions of the $\sqrt{3} \times \sqrt{3}$ MoS$_2$ supercell Brillouin zone and band alignment (vacuum level is set to 0 eV) for MoS$_2$/BAO Z− (a) and Z−↑ (b) heterostructures (without SOC). The red and blue circle dots correspond to the projected band of the MoS$_2$ overlayer on BAO Z− and Z−↑ surfaces and the band structure of the freestanding monolayer MoS$_2$, respectively. Both the black and red short dashed lines indicate the Fermi level.

BAO(0001) substrates,[4,13,43,48] an unusual charge transfer opposite the polarization compensation can be seen in the MoS$_2$ overlayer of the MoS$_2$/BAO Z− heterostructure, as shown in Figure 5. In other words, the MoS$_2$ overlayer on the down-polarized (Z−) ferroelectric BAO(0001) surface is electrostatically n-doped.

As is well known, due to the polarization compensation mechanism, the MoS$_2$ overlayer on the down- and up-polarized ferroelectric surfaces should be electrostatically p- and n-doped, respectively.[4,13,43,48] However, the real situation may be more complex. For example, in refs 49 and 50 as well as in our previous reports[44,51] regarding the graphene/ferroelectric hybrid system, such an unusual charge transfer depending on the surface characteristics of the ferroelectric substrate has also been found. In the final analysis, for the MoS$_2$/BAO Z− heterostructure, the unusual interfacial charge transfer can still be explained in terms of the specific band alignment between the clean BAO Z− polar surface and the freestanding monolayer MoS$_2$. As plotted in Figure 5, the Fermi level of the clean BAO Z− polar surface is 3.37 eV higher than that of the freestanding monolayer MoS$_2$, which inevitably leads to the introduction of n-type carriers in the MoS$_2$ overlayer on the BAO Z− surface. Furthermore, the interfacial charge transfer in the MoS$_2$/BAO Z−↑ heterostructure satisfies the mechanism of band alignment, as plotted in Figure 5. After the charge transfer, the Fermi level of the MoS$_2$/BAO Z−↑ heterostructure is exactly in between the clean BAO Z−↑ polar surface and the freestanding monolayer MoS$_2$. As a result, as mentioned in our previous work,[51] the band alignment between the clean ferroelectric BAO(0001) polar surface and the freestanding monolayer MoS$_2$ should be regarded as a universal mechanism, thereby confirming the interfacial charge transfer in MoS$_2$/BAO(0001) hybrid systems. Indeed, the band alignment between ferroelectric polar surfaces and 2D materials should be a universal criterion determining the interfacial charge transfer in the 2D/ferroelectric hybrid systems.

Finally, the influence of the SOC on the results and conclusions obtained for the MoS$_2$/BAO Z− and Z−↑ heterostructures is explored. As displayed in Figure S2b,d, when the SOC is taken into consideration, the projected bands of the MoS$_2$ overlayer onto the BAO Z− and Z−↑ surfaces undergo downward shifts of 0.90 and 0.74 eV, respectively, which is the same as that of the MoS$_2$ overlayer on the BAO Z− and Z−↑ surfaces without SOC, as shown in Figure 5. In addition to the band-splitting of the VBM, no change can be found in the electronic band structures of the MoS$_2$/BAO Z− and Z−↑ heterostructures with SOC (as shown in Figure S2b,d), which is consistent with the above discussions on the MoS$_2$/BAO Z+ and Z+↓ heterostructures. When the SOC is taken into consideration, the mechanism of band alignment similarly remains valid, as shown in Figure S3c−e.

4. DISCUSSION

First, an important issue is how to construct a thermodynamically favorable 2D/ferroelectric hybrid system using reasonable ferroelectric surface termination. In the material surface and interface science scientific communities, surface reconstruction is a crucial issue. Particularly for a ferroelectric polar surface, the surface stoichiometry, geometry, and electronic structure exhibit a clear dependence on the ferroelectric polarization direction.[52−54] Therefore, it is necessary to use reasonable surface termination in the calculations of 2D/ferroelectric hybrid systems. However, to the best of our knowledge, most existing theoretical calculations regarding 2D/ferroelectric heterostructures have failed to use a system with thermodynamically preferred ferroelectric surface termination.[45,55−59] From the energy difference of the potential well for the $\sqrt{3} \times \sqrt{3}/1 \times 1$ MoS$_2$/BAO(0001) heterostructure before and after polarization reversal, it can be inferred that it is clearly not a reasonable choice to employ a 2D/ferroelectric hybrid system with thermodynamically impossible or nonpreferred ferroelectric surface termination as the preferred system due to the much higher potential energy.

Second, according to the change in carrier type (MoS$_2$ overlayer on the polarization-reversed BAO Z+ surface) or remarkable increase in the carrier density (MoS$_2$ overlayer on the polarization-reversed BAO Z− surface) in the MoS$_2$ overlayer on the BAO(0001) substrate after ferroelectric polarization reversal, the MoS$_2$/BAO(0001) heterostructure is also believed to be promising in MoS$_2$-based FeFET applications. As mentioned in the introduction, for low-power logic applications and nonvolatile memory, FeFETs based on a 2D channel and ferroelectric gating are very attractive candidates owing to the switchable electric polarization and high dielectric constant of ferroelectric materials.[1−5] Additionally, due to the n-type doping in MoS$_2$ overlayers on both BAO Z+ and Z− polar surfaces as well as the respective electrostatically doped p- and n-type MoS$_2$ in the MoS$_2$/BAO Z+↓ and Z−↑ heterostructures, various types of seamless p−i, n−i, p−n, p⁺−p, and n⁺−n homojunctions in monolayer MoS$_2$ on the ferroelectric BAO(0001) polar surface are predicted to occur by reversing the ferroelectric polarization and/or patterning the domain structure. At the same time, the remarkable band offset in the MoS$_2$ monolayer on BAO(0001) substrates with different domain patterns implies that various types of seamless p−i, n−i, p−n, p⁺−p, and n⁺−n homojunctions possessing an extremely steep built-in electric field can be fabricated.[60] As is well known, in modern nanoelectronics and optoelectronics, various p−i, n−i, p−n, p⁺−p, and n⁺−n homo/heterojunctions are fundamental components for realizing the desired functionalities.[61] Such

seamless p−i, n−i, p−n, p⁺−p, and n⁺−n homojunctions in monolayer MoS_2 on the ferroelectric BAO(0001) substrate are very attractive candidates for novel nanoelectronic and optoelectronic devices. Indeed, a p−n homojunction in monolayer $MoTe_2$ on a periodically polarized ferroelectric P(VDF-TrFE) substrate has been already experimentally prepared.[13] In addition, by patterning the domain structures of a ferroelectric $LiNbO_3$(0001) substrate, periodic arrays of a p−i homojunction in a graphene channel have been confirmed.[45]

Third, different from the polarization compensation mechanism, in the MoS_2/BAO Z− heterostructure, an unusual interfacial charge transfer is found, i.e., an electrostatically doped n-type MoS_2 overlayer on the down-polarized (Z−) ferroelectric BAO(0001) surface. As mentioned above, due to the polarization compensation mechanism, the MoS_2 overlayer on down- and up-polarized ferroelectric surfaces is usually electrostatically p- or n-doped, respectively. Although the doping carrier type in the MoS_2 overlayer on the BAO Z+, Z+↓, and Z−↑ polar surfaces satisfies the mechanism of polarization compensation, in the final analysis, the universal mechanism determining the interfacial charge transfer should be attributed to the specific band alignment between the clean BAO(0001) substrate and the freestanding monolayer MoS_2 due to the unusual interfacial charge transfer in the MoS_2/BAO Z− hybrid system. Indeed, the band alignment method has been used to explain charge doping in graphene on a ferroelectric $SrTiO_3$(111) substrate.[62] In our former studies regarding graphene/BAO(0001) hybrid systems and 1T-VSe_2/$BiFeO_3$(0001) heterostructures,[51,63] such a mechanism has also been confirmed. As a result, the band alignment between ferroelectric polar surfaces and 2D materials should be a universal criterion determining the interfacial charge transfer in 2D/ferroelectric heterostructures.

Finally, it is worth mentioning that in the present work, only the intrinsic interface coupling and electrostatic modulation were explored in the MoS_2/BAO(0001) heterostructure excluding adsorbates (contaminants) and defects. However, in experiments, 2D monolayer materials are usually transferred onto a clean single-crystal ferroelectric substrate using a one-touch wet transfer method,[45] which inevitably introduces OH^-, H^+, or even a defective MoS_2/BAO(0001) interface, i.e., interfacial adsorbates (contaminants) and defects. For actual MoS_2/BAO(0001) hybrid systems, these interfacial adsorbates (contaminants) and defects can play a key role in the interfacial charge transfer process.[45,49,50,57] In other words, for the real systems, due to the existence of adsorbates (contaminants) as well as defects, various surface reconstructions may take place, which will inevitably lead to more complicated situations. For example, experimental observations show that surface characteristics and adsorbates (contaminants) play an important role in the electrostatic doping of graphene on ferroelectric polar surfaces. As reported in ref 50, for graphene-based FeFETs with La-doped PZT gating, the intrinsic resistance change shows an antihysteresis behavior when the adsorbed molecules are removed via a vacuum annealing process. In addition, in ref 49, a transformation from a ferroelectric hysteresis to an antihysteresis was observed in the graphene channel for the adsorbate-removed graphene/ferroelectric hybrid system using superlattice $PbTiO_3$/$SrTiO_3$ substrates with different surface characteristics. Therefore, the extrinsic effect of adsorbates (contaminants) and defects at the MoS_2/BAO(0001) interface deserves further exploration.

5. CONCLUSIONS

In conclusion, based on the thermodynamically preferred ferroelectric BAO(0001) polar surfaces, we investigated the intrinsic interface coupling and electrostatic modulation as well as the effect of ferroelectric polarization reversal in a MoS_2/BAO(0001) heterostructure via first-principles DFT calculations. First, our study points out that to construct a thermodynamically favorable 2D/ferroelectric hybrid system, thermodynamically preferred ferroelectric surface termination should be an important prerequisite. Second, the effect of the ferroelectric polarization reversal of the BAO(0001) substrate, the n-type doping in the MoS_2 overlayers on both the BAO Z+ and Z− polar surfaces, and the respective electrostatically doped p- and n-type MoS_2 in the MoS_2/BAO Z+↓ and Z−↑ heterostructures show that the MoS_2/BAO(0001) heterostructure holds much promise for MoS_2-based FeFETs. Furthermore, this heterostructure could be a potential candidate for the application of various types of seamless p−i, n−i, p−n, p⁺−p, and n⁺−n homojunctions possessing an extremely steep built-in electric field. Third, different from the polarization compensation, in the final analysis, the potential physical mechanism determining the interfacial charge transfer in the MoS_2/BAO(0001) heterostructure should be attributed to the specific band alignment between the clean BAO(0001) substrate and the freestanding monolayer MoS_2. This should be regarded as a universal criterion dictating the interfacial charge transfer in 2D/ferroelectric heterostructures. Finally, the interaction mechanism of the large ionic−vdW coupling in MoS_2/BAO(0001) heterostructures should also be an important point worth considering.

◼ ASSOCIATED CONTENT

ⓈI Supporting Information

The Supporting Information is available free of charge at https://pubs.acs.org/doi/10.1021/acsomega.1c03556.

> Further details on the top views of respective five typical interfacial configurations for MoS_2/BAO Z+ and MoS_2/BAO Z− heterostructures, band structures along high-symmetry directions of the $\sqrt{3} \times \sqrt{3}$ MoS_2 supercell Brillouin zone for MoS_2/BAO Z+, Z+↓, Z−, and Z−↑ heterostructures (with SOC), band alignment between the freestanding monolayer MoS_2 and clean BAO(0001) substrate (with SOC), side views of atomic structures, ELFs, and differential charge densities as well as the energy difference (ΔE) of the potential well for $\sqrt{3} \times \sqrt{3}/1 \times 1$ MoS_2/BAO Z− and Z−↑ heterostructures, and side views of ELFs for the clean BAO Z+, Z + ↓, Z−, and Z−↑ surfaces (PDF)

◼ AUTHOR INFORMATION

Corresponding Author

Jian-Qing Dai − *Faculty of Materials Science and Engineering, Kunming University of Science and Technology, Kunming 650093, P. R. China;* ⓞ orcid.org/0000-0003-4352-0789; Email: djqkust@sina.com

Authors

Jin Yuan − *Faculty of Materials Science and Engineering, Kunming University of Science and Technology, Kunming 650093, P. R. China*

Cheng Ke − *Faculty of Materials Science and Engineering, Kunming University of Science and Technology, Kunming 650093, P. R. China*

Complete contact information is available at:
https://pubs.acs.org/10.1021/acsomega.1c03556

Notes

The authors declare no competing financial interest.

REFERENCES

(1) Liu, X.; Zhou, X.; Pan, Y.; Yang, J.; Xiang, H.; Yuan, Y.; Liu, S.; Luo, H.; Zhang, D.; Sun, J. Charge-ferroelectric transition in ultrathin $Na_{0.5}Bi_{4.5}Ti_4O_{15}$ flakes probed via a dual-gated full van der Waals transistor. *Adv. Mater.* **2020**, *32*, 2004813.

(2) Cha, M.-Y.; Liu, H.; Wang, T.-Y.; Chen, L.; Zhu, H.; Ji, L.; Sun, Q.-Q.; Zhang, D. W. MoS_2-based ferroelectric field-effect transistor with atomic layer deposited $Hf_{0.5}Zr_{0.5}O_2$ films toward memory applications. *AIP Adv.* **2020**, *10*, No. 065107.

(3) Lipatov, A.; Sharma, P.; Gruverman, A.; Sinitskii, A. Optoelectrical molybdenum disulfide (MoS_2)-ferroelectric memories. *ACS Nano* **2015**, *9*, 8089−8098.

(4) Jie, W.; Hui, Y.-Y.; Chan, N.-Y.; Zhang, Y.; Lau, S. P.; Hao, J. Ferroelectric polarization effects on the transport properties of graphene/PMN-PT field effect transistors. *J. Phys. Chem. C* **2013**, *117*, 13747−13752.

(5) Rogers, S. P.; Xu, R.; Pandya, S.; Martin, L. W.; Shim, M. Slow conductance relaxation in graphene-ferroelectric field-effect transistors. *J. Phys. Chem. C* **2017**, *121*, 7542−7548.

(6) Hong, X.; Hoffman, J.; Posadas, A.; Zou, K.; Ahn, C. H.; Zhu, J. Unusual resistance hysteresis in n-layer graphene field effect transistors fabricated on ferroelectric $Pb(Zr_{0.2}Ti_{0.8})O_3$. *Appl. Phys. Lett.* **2010**, *97*, No. 033114.

(7) Zhang, X. W.; Xie, D.; Xu, J. L.; Sun, Y. L.; Li, X.; Zhang, C.; Dai, R. X.; Zhao, Y. F.; Li, X. M.; Li, X. MoS_2 field-effect transistors with lead zirconate-titanate ferroelectric gating. *IEEE Electron Device Lett.* **2015**, *36*, 784−786.

(8) Ko, C.; Lee, Y.; Chen, Y.; Suh, J.; Fu, D.; Suslu, A.; Lee, S.; Clarkson, J. D.; Choe, H. S.; Tongay, S.; Ramesh, R.; Wu, J. Ferroelectrically gated atomically thin transition-metal dichalcogenides as nonvolatile memory. *Adv. Mater.* **2016**, *28*, 2923−2930.

(9) Li, C. H.; McCreary, K. M.; Jonker, B. T. Spatial control of photoluminescence at room temperature by ferroelectric domains in monolayer WS_2/PZT hybrid structures. *ACS Omega* **2016**, *1*, 1075−1080.

(10) Silva, J. P.; Marques, B. C. A.; Moreira, J. A.; Conde, O. Resistive switching in $MoSe_2$/$BaTiO_3$ hybrid structures. *J. Mater. Chem. C* **2017**, *5*, 10353−10359.

(11) Preciado, E.; Schülein, F. J. R.; Nguyen, A. E.; Barroso, D.; Isarraraz, M.; von Son, G.; Lu, I.-H.; Michailow, W.; Möller, B.; Klee, V.; Mann, J.; Wixforth, A.; Bartels, L.; Krenner, H. J. Scalable fabrication of a hybrid field-effect and acousto-electric device by direct growth of monolayer MoS_2/$LiNbO_3$. *Nat. Commun.* **2015**, *6*, 8593−8600.

(12) Lu, Z.; Serrao, C.; Khan, A. I.; You, L.; Wang, J. C.; Ye, Y.; Zhu, H.; Zhang, X.; Salahuddin, S. Nonvolatile MoS_2 field effect transistors directly gated by single crystalline epitaxial ferroelectric. *Appl. Phys. Lett.* **2017**, *111*, No. 023104.

(13) Wu, G.-J.; Wang, X.-G.; Chen, Y.; Wu, S.-Q.; Wu, B.; Jiang, Y.; Shen, H.; Lin, T.; Liu, Q.; Wang, X.; Zhou, P.; Zhang, S.; Hu, W.; Meng, X.; Chu, J.; Wang, J. $MoTe_2$ p-n homojunctions defined by ferroelectric polarization. *Adv. Mater.* **2020**, *32*, 1907937.

(14) Mak, K. F.; Lee, C.; Hone, J.; Shan, J.; Heinz, T. F. Atomically thin MoS_2: A new direct-gap semiconductor. *Phys. Rev. Lett.* **2010**, *105*, 136805.

(15) Yu, Y.; Yu, Y.; Cai, Y.; Li, W.; Gurarslan, A.; Peelaers, H.; Aspnes, D. E.; Van de Walle, C. G.; Nguyen, N. V.; Zhang, Y. W.; Cao, L. Exciton-dominated dielectric function of atomically thin MoS_2 films. *Sci. Rep.* **2015**, *5*, 16996.

(16) Guan, G.; Zhang, S.; Liu, S.; Cai, Y.; Low, M.; Teng, C. P.; Phang, I. Y.; Cheng, Y.; Duei, K. L.; Srinivasan, B. M.; Zheng, Y.; Zhang, Y. W.; Han, M. Y. Protein induces layer-by-layer exfoliation of transition metal dichalcogenides. *J. Am. Chem. Soc.* **2015**, *137*, 6152−6155.

(17) Wang, S.; Wang, X.; Warner, J. H. All chemical vapor deposition growth of MoS_2: h-BN vertical van der Waals heterostructures. *ACS Nano* **2015**, *9*, 5246−5254.

(18) Ren, K.; Sun, M. L.; Luo, Y.; Wang, S. K.; Yu, J.; Tang, W. C. First-principle study of electronic and optical properties of two-dimensional materials-based heterostructures based on transition metal dichalcogenides and boron phosphide. *Appl. Surf. Sci.* **2019**, *476*, 70−75.

(19) Belik, A. A.; Wuernisha, T.; Kamiyama, T.; Mori, K.; Maie, M.; Nagai, T.; Matsui, Y.; Takayama-Muromachi, E. High-pressure synthesis, crystal structures, and properties of perovskite-like $BiAlO_3$ and pyroxene-like $BiGaO_3$. *Chem. Mater.* **2006**, *18*, 133−139.

(20) Wang, H.; Wang, B.; Li, Q.; Zhu, Z.; Wang, R.; Woo, C. H. First-principles study of the cubic perovskites $BiMO_3$ (M = Al, Ga, In, and Sc). *Phys. Rev. B* **2007**, *75*, 245209.

(21) Zylberberg, J.; Belik, A. A.; Takayama-Muromachi, E.; Ye, Z. G. Bismuth ALUMINATE: A NEW high-T_C lead-free piezo−/ferro-electric. *Chem. Mater.* **2007**, *19*, 6385−6390.

(22) Dai, J.-Q.; Wang, X.-W.; Xu, J.-W. Polarization direction dependence of thermodynamic stability of ferroelectric $BiAlO_3$(0001) polar surfaces. *J. Phys. Chem. C* **2018**, *122*, 29220−29227.

(23) Son, J. Y.; Oark, C. S.; Shin, Y. H. Epitaxial thin film as a lead-free ferroelectric material. *Appl. Phys. Lett.* **2008**, *92*, 222911.

(24) da Silveira, L. G. D.; Barone, P.; Picozzi, S. Rashba-Dresselhaus spin-splitting in the bulk ferroelectric oxide $BiAlO_3$. *Phys. Rev. B* **2016**, *93*, 245159.

(25) Dai, J.-Q.; Yuan, J. Distinctive electronic and spin structures at the oppositely polarized ferroelectric $BiAlO_3$(0001) surfaces. *Appl. Surf. Sci.* **2019**, *481*, 702−711.

(26) Kresse, G.; Furthmüller, J. Efficient iterative schemes for Ab initio total-energy calculations using a plane-wave basis set. *Phys. Rev. B: Condens. Matter Mater. Phys.* **1996**, *53*, 11169.

(27) Blöchl, P. E. Projector augmented-wave method. *Phys. Rev. B: Condens. Matter Mater. Phys.* **1994**, *50*, 17953.

(28) Kresse, G.; Joubert, J. From ultrasoft pseudopotentials to the projector augmented-wave method. *Phys. Rev. B: Condens. Matter Mater. Phys.* **1999**, *59*, 1758.

(29) Perdew, J. P.; Ruzsinszky, A.; Csonka, G. I.; Vydrov, O. A.; Scuseria, G. E.; Constantin, L. A.; Zhou, X. L.; Burk, K. Restoring the density-gradient expansion for exchange in solids and surfaces. *Phys. Rev. Lett.* **2008**, *100*, 136406.

(30) Grimme, S.; Ehrlich, S.; Goerigk, L. Effect of the damping function in dispersion corrected density functional theory. *J. Comput. Chem.* **2011**, *32*, 1456−1465.

(31) Yu, M.; Trinkle, D. R. Accurate and efficient algorithm for Bader charge integration. *J. Chem. Phys.* **2011**, *134*, No. 064111.

(32) Makov, G.; Payne, M. C. Periodic boundary conditions in ab initio calculations. *Phys. Rev. B: Condens. Matter Mater. Phys.* **1995**, *51*, 4014.

(33) Cai, Y.; Lan, J.; Zhang, G.; Zhang, Y.-W. Lattice vibrational modes and phonon thermal conductivity of monolayer MoS_2. *Phys. Rev. B* **2014**, *89*, No. 035438.

(34) Xiao, Z.; Song, J.; Ferry, D. K.; Ducharme, S.; Hong, X. Ferroelectric-domain-patterning-controlled schottky junction state in monolayer MoS_2. *Phys. Rev. Lett.* **2017**, *118*, 236801.

(35) Cheng, C.; Sun, J.-T.; Chen, X.-R.; Fu, H.-X.; Meng, S. Nonlinear Rashba spin splitting in transition metal dichalcogenide monolayers. *Nanoscale* **2016**, *8*, 17854−17860.

(36) Finnis, M. W. The theory of metal−ceramic interfaces. *J. Phys.: Condens. Matter* **1996**, *8*, 5811.

(37) Liu, Y.; Huang, Y.; Duan, X.-F. Van der Waals integration before and beyond two-dimensional materials. *Nature* **2019**, *567*, 323−333.

(38) Yakovkin, I. Interlayer interaction and screening in MoS_2. *Surf. Rev. Lett.* **2014**, *21*, 1450039.

(39) Liu, Z. J.-Z.; Cheng, Y. Interlayer binding energy of graphite: A mesoscopic determination from deformation. *Phys. Rev. B* **2012**, *85*, 205418.

(40) Becke, A. D.; Edgecombe, K. E. A simple measure of electron localization in atomic and molecular systems. *J. Chem. Phys.* **1990**, *92*, 5397−5403.

(41) Silvi, B.; Savin, A. Classification of chemical bonds based on topological analysis of electron localization functions. *Nature* **1994**, *371*, 683−686.

(42) Bae, S.-H.; Kum, H.; Kong, W.; Kim, Y.; Choi, C.; Lee, B.; Lin, P.; Park, Y.; Kim, J. Integration of bulk materials with two-dimensional materials for physical coupling and applications. *Nat. Mater.* **2019**, *18*, 550−560.

(43) Dai, J.-Q.; Li, X.-Y.; Xu, J.-W. Charge doping in graphene on thermodynamically preferred $BiFeO_3(0001)$ polar surfaces. *Phys. Chem. Chem. Phys.* **2017**, *19*, 31352−31361.

(44) Dai, J.-Q.; Cao, T.-F.; Wang, X.-W. Effect of surface termination on charge doping in graphene/$BiFeO_3(0001)$ hybrid structure. *J. Phys. Chem. C* **2018**, *122*, 17250−17260.

(45) Baeumer, C.; Saldana-Greco, D.; Martirez, J. M. P.; Rappe, A. M.; Shim, M.; Martin, L. W. Ferroelectrically driven spatial carrier density modulation in graphene. *Nat. Commun.* **2015**, *6*, 6136.

(46) Liu, Y.; Guo, J.; Zhu, E.; Liao, L.; Lee, S.-J.; Ding, M.; Shakir, I.; Gambin, V.; Huang, Y.; Duan, X. Approaching the Schottky-Mott limit in van der Waals metal-semiconductor junctions. *Nature* **2018**, *557*, 696−700.

(47) Medeiros, P. V. C.; Stafström, S.; Björk, J. Effects of extrinsic and intrinsic perturbations on the electronic structure of graphene: retaining an effective primitive cell band structure by band unfolding. *Phys. Rev. B: Condens. Matter Mater. Phys.* **2014**, *89*, No. 041407.

(48) Baeumer, C.; Rogers, S. P.; Xu, R.; Martin, L. W.; Shim, M. Tunable carrier type and density in graphene/$PbZr_{0.2}Ti_{0.8}O_3$ hybrid structures through ferroelectric switching. *Nano Lett.* **2013**, *13*, 1693−1698.

(49) Yusuf, M. H.; Nielsen, B.; Dawber, M.; Du, X. Extrinsic and intrinsic charge trapping at the graphene/ferroelectric interface. *Nano Lett.* **2014**, *14*, 5437−5444.

(50) Ma, C.; Gong, Y.; Lu, R.; Brown, E.; Ma, B.; Li, J.; Wu, J. Detangling extrinsic and intrinsic hysteresis for detecting dynamic switch of electric dipoles using graphene field-effect transistors on ferroelectric gates. *Nanoscale* **2015**, *7*, 18489−18497.

(51) Yuan, J.; Dai, J.-Q.; Ke, C.; Wei, Z.-C. Interface coupling and charge doping in graphene on ferroelectric $BiAlO_3(0001)$ polar surfaces. *Phys. Chem. Chem. Phys.* **2021**, *23*, 3407−3416.

(52) Goniakowski, J.; Finocchi, F.; Noguera, C. Polarity of oxide surfaces and nanostructures. *Rep. Prog. Phys.* **2008**, *71*, No. 016501.

(53) Kakekhani, A.; Ismail-Beigi, S.; Altman, E. I. Ferroelectrics: A pathway to switchable surface chemistry and catalysis. *Surf. Sci.* **2016**, *650*, 302−316.

(54) Khan, M. A.; Nadeem, M. A.; Idrissn, H. Ferroelectric polarization effect on surface chemistry and photoCatalytic activity: A review. *Surf. Sci. Rep.* **2016**, *71*, 1−31.

(55) Ding, J.; Wen, L.-W.; Li, H.-D.; Kang, X.-B.; Zhang, J.-M. First-principles investigation of graphene on the ferroelectric $LiNbO_3(001)$ surface. *Europhys. Lett.* **2013**, *104*, 17009.

(56) Belletti, G. D.; Dalosto, S. D.; Tinte, S. Ferroelectric surface induced electron doping in a zigzag graphene nanoribbon. *J. Phys.: Condens. Matter* **2016**, *28*, 435002.

(57) Yue, C.; Lu, X.; Zhang, J.; Huang, F.; Zhu, J. Electrostatic doping of graphene from a $LiNbO_3(0001)$ substrate. *J. Phys. D: Appl. Phys.* **2021**, *54*, 235303.

(58) Sanna, S.; Schmidt, W. G. Lithium niobate X-cut, Y-cut, and Z-cut surfaces from Ab initio theory. *Phys. Rev. B: Condens. Matter Mater. Phys.* **2010**, *81*, 214116.

(59) Garrity, K.; Kakekhani, A.; Kolpak, A.; Ismail-Beigi, S. Ferroelectric surface chemistry: first-principles study of the $PbTiO_3$ surface. *Phys. Rev. B: Condens. Matter Mater. Phys.* **2013**, *88*, No. 045401.

(60) Catalan, G.; Seidel, J.; Ramesh, R.; Scott, J. F. Domain wall nanoelectronics. *Rev. Mod. Phys.* **2012**, *84*, 119−156.

(61) Neamen, D. A. *Semiconductor physics and devices: Basic principles*; McGraw-Hill, 2011.

(62) Shin, D.; Demkov, A. A. Theoretical investigation of the band alignment of graphene on a polar $SrTiO_3(111)$ surface. *Phys. Rev. B: Condens. Matter Mater. Phys.* **2018**, *97*, No. 075423.

(63) Dai, J.-Q.; Yuan, J.; Ke, C.; Wei, Z.-C. Tunable electronic and magnetic properties in $1 T$-VSe_2 monolayer on $BiFeO_3(0001)$ ferroelectric substrate. *Appl. Surf. Sci.* **2021**, *547*, 149206.